Physics of Plasmas

RESEARCH ARTICLE | JUNE 05 2024

Space-resolved electron density and temperature evaluation by x-ray pinhole camera method in an ECR plasma

G. Finocchiaro ; E. Naselli ; B. Mishra ; S. Biri ; M. Mazzaglia ; A. Pidatella ; R. Rácz ; G. Torrisi ; D. Mascali

Phys. Plasmas 31, 062506 (2024)
https://doi.org/10.1063/5.0207185

Space-resolved electron density and temperature evaluation by x-ray pinhole camera method in an ECR plasma

Cite as: Phys. Plasmas **31**, 062506 (2024); doi: 10.1063/5.0207185
Submitted: 6 March 2024 · Accepted: 21 May 2024 ·
Published Online: 5 June 2024

G. Finocchiaro,[1,2,a)] E. Naselli,[2] B. Mishra,[1,2] S. Biri,[3] M. Mazzaglia,[2] A. Pidatella,[2] R. Rácz,[3] G. Torrisi,[2] and D. Mascali[2]

AFFILIATIONS

[1]Dipartimento di Fisica e Astronomia, Università degli Studi di Catania, 95125 Catania, Italy
[2]INFN-Laboratori Nazionali del Sud, 95125 Catania, Italy
[3]Institute for Nuclear Research (Atomki), 4026 Debrecen, Hungary

[a)]Author to whom correspondence should be addressed: giorgio.finocchiaro@lns.infn.it

ABSTRACT

X-ray emission characterization provides valuable insights about electron cyclotron resonance (ECR) plasmas. In principle, space-resolved spectroscopic techniques can be used to reveal spatial distributions of electron density and temperature. In the PANDORA (Plasma for Astrophysics, Nuclear Decay Observation, and Radiation for Archaeometry) project framework, and within the collaboration between the Atomki and INFN-LNS laboratories, we developed a high-resolution full-field x-ray pinhole setup. This setup incorporates advanced analysis techniques for single photon counted imaging in high dynamical range mode, enabling x-ray imaging and space-resolved spectroscopy at high spatial and energy resolution (560 μm and 242 eV @ 8.1 keV, respectively). Here, we introduce an innovative technique for quantitatively evaluating the local electron density and temperature of plasma, as the first application of such a method in an ECR setup. Specifically, we examine an argon plasma heated by 200 W microwave power at 14 GHz. Our analysis includes a retrospective comparison with past x-ray data collected from other ECR ion source setups. Our findings clearly reveal the formation of a plasmoid–halo structure within the plasma chamber, characterized by a dense and hot plasma almost totally enclosed inside the ECR magnetic iso-surface (the plasmoid). This plasmoid exhibits nearly uniform distribution of electron density and temperature, with only gentle gradients of both the parameters toward its edges. Inside the halo, x-ray emission is minimal or even negligible. Notably, cusp structures correspond to magnetic branches where deconfined electrons impinge upon the plasma chamber walls and endplates. The average values of temperature and density measured inside the plasmoid are 12.44 ± 1.84 keV and $(1.66 \pm 0.15) \times 10^{17}$ m^{-3}, respectively.

I. INTRODUCTION

The use of x-ray diagnostics as a non-invasive tool to study hot plasmas is well known in the literature, both for ion sources and plasma-based fusion facilities.[1]

A crucial point in their application for energetic plasmas is related to the opportunity to make non-intrusive, quantitative analysis of the thermodynamic plasma parameters, namely, electron density and temperature.

Energy-resolved measurements performed on electron cyclotron resonance ion source (ECRIS) plasmas allowed us to characterize the bremsstrahlung emission,[2–4] thus determining the spectral temperature of the electrons, by analyzing the electron energy distribution function (EEDF) with appropriate plasma emissivity models.[5]

Space-resolved measurements performed by pinhole-based imaging techniques enabled the morphologic study of different kinds of plasmas.[6–9] These techniques have allowed us along the years to investigate the three dimensional (3D) structures of various kinds of magnetically confined plasmas, evidencing their overall structure and the spatial distribution of the warmer electrons, which play a main role in leading to x-ray emission via characteristic lines and bremsstrahlung radiation.

This work is focused on the study of ECR plasmas generated in B-minimum magnetic structures traditionally adopted as ECRIS. In particular, a quantitative space-resolved analysis of plasma x-ray emissivity was developed, which allowed us to evaluate the spatial distribution of electron temperature and plasma density.

Most of the available spectroscopy studies on ECR plasmas rely on volumetric measurements, i.e., the total x-ray flux emitted from the plasma along a given cone-of-view, normally individuated by proper collimation systems, which are widely performed to characterize the EEDF from mostly the bremsstrahlung emission.[5,10,11] However, these plasmas being in non-LTE (local thermodynamic equilibrium) conditions, the method is strongly affected by EED anisotropy and deviation from a single Maxwellian slope: actual ECRIS EEDF are in fact characterized by the presence of different electron populations (cold, warm, and hot), each one contributing to the overall distribution function, which assumes the typical three-slope structure,[12] and whose experimental decoupling represents a criticality of any diagnostic setup.

An additional limitation in the use of simplified volumetric setups for the x-ray diagnostics comes from the difficult decoupling of the pure plasma-emitted radiation from the x rays coming from the plasma chamber walls, typically made of stainless steel or other metals. Fluxes of deconfined electrons also contribute to bremsstrahlung radiation, and even this emission is comparatively larger than the one coming from the plasma core directly, due to the higher density of solids composing the chamber walls. The mixing of both plasma and plasma chamber wall contributions seriously affects the reliability of volumetric measurements when collimators are not properly designed and shaped in order to totally suppress the unwanted contributions.

To deal with this important issue, several measurements have been performed by using on-purpose developed collimators, to have cones-of-view intercepting specific portions of the plasma (typically, the plasma core).[5,13]

A significant step forward, improving by far the reliability of a real plasma x-ray flux measurement, without significant contribution from the plasma chamber walls, can be done by using position-sensitive detectors, such as charge coupled devices (CCD), coupled to pinholes.[14] This "camera-obscura"-like setup enables, under appropriate experimental techniques and with sophisticated post-processing procedures, both energy and space-resolved measurements: in this way, having the opportunity to collect spatial images of the plasma under different excitation conditions, it is directly possible to individuate the signal coming from the confined plasma vs deconfined plasma fluxes.

In particular, the x-ray imaging focused on the characteristic line emission of plasma atomic species gives access to information about in-plasma ion distribution; moreover the deconfined electron fluxes are made evident by the characteristic line emission of the metals in the chamber walls, induced by the electrons' impact.[15,16]

As reported in Mascali *et al.*,[17] x-ray-integrated imaging measurements have been performed using a CCD detector, obtaining a map of confined and deconfined plasma under different plasma tuning conditions [e.g., single vs double frequency heating, radio frequency (RF) power and frequency scaling, and background pressure].

Due to the lack of precise measurements on warm electron-driven plasma radiation (1–30 keV), only few data about absolute values of plasma density and temperature in an ECR setup are nowadays available.[18] The typical CCD detector sensitivity range (2–20 keV) suites very well for probing the warm electron plasma parameters, whose related spatial distribution affects the ion charge state distribution (CSD). The overall performances of an ECRIS can be strongly influenced by the latter quantity.

Coupling the energy-resolved x-ray measurement with the x-ray CCD imaging turns out to be a powerful technique: the quantitative evaluation of the experimental x-ray spectra can be provided in a space-resolved way, by means of the single photon counting (SPhC) acquisition mode.

Such a technique was applied in Naselli *et al.*,[15] by developing a specific post-processing algorithm described in detail in the publication. The energy and position of each single photon is collected in a full-field view of the plasma, thus producing a 2D x-ray plasma image, preserving the energy information and the absolute brightness in each pixel (i.e., number of photons per second, per cm^2). Consequently, this enables the local estimation of the plasma parameters (electron density and temperature) and spectral composition investigations in different regions inside the plasma chamber.

The post-processing algorithm also provides the application of a high dynamical range (HDR) imaging technique, which is needed due to the observed differences of several orders of magnitude in the plasma emissivity.

In this paper, we describe an experimental technique for the evaluation of local warm electron temperature and density, performed on an ECR argon plasma, heated by 200 W microwave power in the 14 GHz ECR ion source (Atomki–Debrecen, Hungary).

II. EXPERIMENTAL SETUP

The sketch of the experimental setup is shown in Fig. 1. The measurements were carried out in the ECR Laboratory of Atomki–Debrecen (Hungary), in a B-minimum plasma trap especially designed for research aims.[19] An argon plasma was excited by the injection of a 14.25 GHz RF pumping frequency, with a net power of 200 W. Net power means that forward and reflected power were, from time to time and from one datapoint to another, adjusted in order to keep their net difference as equal to 200 W within 1% of fluctuation. These operative settings are reported in Table I.

A special design of the plasma chamber was implemented for the purpose of this experiment: the metallic chamber walls, made of stainless steel, were covered by liners of different metals, which were selected in order to generate specific x-ray fluorescence peaks induced by the electron fluxes escaping from the magnetic trap.

In particular, the lateral wall of the cylindrical chamber was covered by a tantalum (Ta) liner ($E_{L\alpha} = 8.15$ keV) and the extraction endplate was covered by titanium (Ti) ($E_{K\alpha} = 4.51$ keV). The x-ray view line was obtained through an aluminum (Al) mesh placed on the injection endplate, also working as a Faraday screen, which guarantees a proper enclosure of the chamber that acts as a resonant cavity for the microwaves. The mesh covered almost two thirds of the endplate, while the rest was made of bulk Al, in order to host the gas pipe and the waveguide (as shown in Fig. 1).

The space-resolved detection of Ti and Ta spectral lines, together with the ones produced by the Ar ions of the plasma ($E_{K\alpha} = 2.96$ keV), gave the whole (longitudinally integrated) 2D map of the x-ray emissivity.

The Pb pinhole was placed in between two lead collimating disks, that were located at distances of $l_1 = 40$ mm far from the pinhole at the CCD side, and $l_2 = 6$ mm far from the pinhole at the plasma side. The optical magnification was optimized at M = 0.244 (distance pinhole–CCD = 232 mm, distance pinhole–plasma center = 952 mm).

The exposure time of the CCD was set according to the overall brightness of the plasma, but anyway in order to operate in SPhC on the largest part of the CCD active area. Due to the extreme variability of the x-ray flux from point to point, especially between the plasma

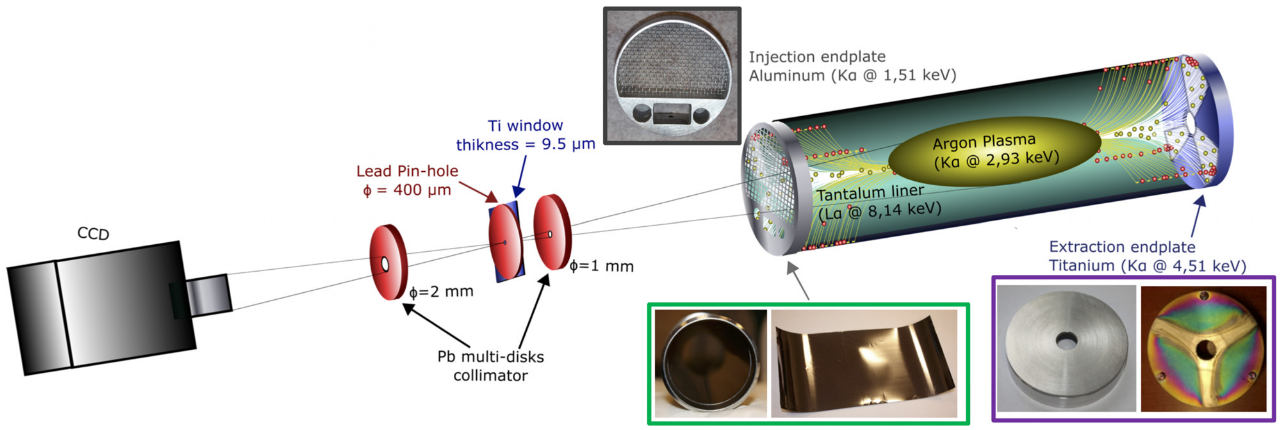

FIG. 1. Sketch of the experimental setup. From the left: CCD camera, pinhole multi-collimator system, plasma chamber coated with tantalum liner, and closed by aluminum mesh and a titanium electrode.

TABLE I. Operative settings of the ECR experimental setup.

RF power	RF frequency	Gas type	Gas pressure
200 W	14.25 GHz	Ar	2.2×10^{-6} mbar

core and plasma chamber walls, it was not possible to select just a single exposure time, capable to provide single photon counting conditions on the whole image. The raw images at large exposure times demonstrated that the emissivity dynamical range was huge, differing in several orders of magnitudes in intensity. Hence, similar to classical photography, a HDR mode and analysis was implemented. Two sets of multiple frames were acquired: one of 3000 frames, at exposure time $T_\epsilon = 0.7$ s, and a second one made of 1000 frames at $T_\epsilon = 0.05$ s, more suitable for the brightest parts of the image. In this way, we were able to get, by means of an advanced analytical method applied during the image post-processing, a weighted convoluted image.

In addition to the CCD camera, an SDD (silicon drift detector, XGL-SPCM-8110-CUBE) was coupled alternatively to the pinhole in the same optical arrangement, and it was used for benchmark and reference acquisitions, to correct the unwanted effects induced by the post-processing analysis as described in detail in Sec. III A.

As the SDD was not suitable to be placed in vacuum, it was coupled to the vacuum system by a Kapton window of 50 μm thickness (Fig. 2).

The SDD and CCD intrinsic quantum efficiencies, taking into account the x-ray transparency, including the Ti window for the CDD and the Kapton plus Ti for the SDD, are shown in Fig. 3.

III. SINGLE PHOTON COUNTING DATA POST-PROCESSING

A specific analysis algorithm was developed for processing the single photon counted output of the x-ray detector and, thus, obtaining the energy and space-resolved information.[15,16]

In a nutshell, it consists of the four following main sequential steps:

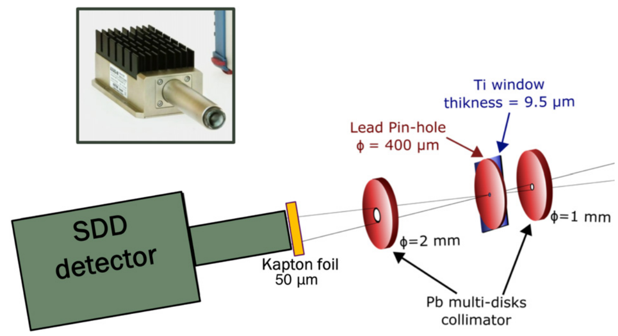

FIG. 2. SDD detector mounted alternately on the same field of view of the CCD camera. The 50 μm Kapton foil couples the detector with the vacuum system.

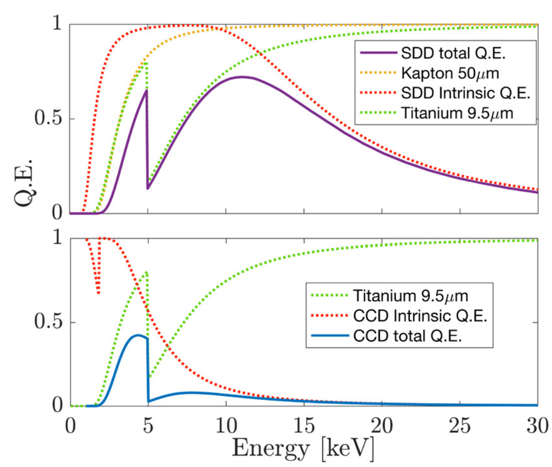

FIG. 3. Quantum efficiencies of the SDD and CCD detectors including the windows used in the two cases: Ti and Kapton for the SDD, Ti only for the CCD setup.

(A) Cluster grouping: i.e., identification and integration of pixel clusters belonging to single photon impact events;
(B) HDR imaging convolution: properly weighted summation of images acquired at different exposure times;
(C) Readout noise reconstruction and removal;
(D) Energy calibration.

The *cluster grouping* (A) algorithm processes all the acquired data frames and it is based on the MATLAB-based graphical recognition of "clusters" in a sparse matrix. These clusters are normally groups of pixels activated by each single photon event, which contain the energy and position information of the impinging radiation.[15] The reason for this behavior is due to the charge drift processes in the silicon CCD detector.[20,21] An example of the sparse image matrix is shown in Fig. 4. This algorithm also identifies and reduces pileup events generated by multiple photons impinging on the same cluster of pixels. The result of this sequence of processes is the collected SPhC array including two spatial coordinates and the corresponding energy information.

The *second step* (B) consists of the convolution of two different datasets [Figs. 5(a) and 5(b)], acquired under different exposure conditions (see Table II), in order to produce a single HDR energy-resolved image [Fig. 5(c)], containing an x-ray energy spectrum on each pixel. The convolution is weighted by the pileup rate map of the long-exposure dataset.[16]

The *step* (C) aims to remove the effect induced by the sequential readout process of the CCD (whose mechanism is explained in detail in Naselli *et al.*[15]); as the CCD is still active during the array readout, the raw data contain unwanted information collected during the movement and collection of the charges along the sensor, producing a characteristic "strip" in each of the image frames.

A proper algorithm has been developed to manage this effect as well, in order to reconstruct the inverse reading process and reallocate the photons collected during the readout phase in their correct positions, as shown in Fig. 6.

The *energy calibration* (D) is performed by an accurate identification of the main characteristic lines on the spectra in the range of $4.5 - 11\,\mathrm{keV}$, which is possible by investigating the reconstructed photon-counted HDR image and focusing on the space-resolved information.

Figure 7 shows the Ta-$L\alpha$ characteristic line at 8.15 keV, on which the energy resolution was estimated at 242 eV.

Despite the above-mentioned exposure times being accurately determined to assure single photon events, a careful analysis of the frames put in evidence that a certain fraction of detected events are made of overlapped photons. The post-processing algorithm is also capable of discarding such unwanted events, even though with an efficiency less than 100%. In order to correct additional spurious results coming from the post-processing of the raw data, which may affect the reliability of the energy spectra, we developed an additional benchmark procedure that is described below.

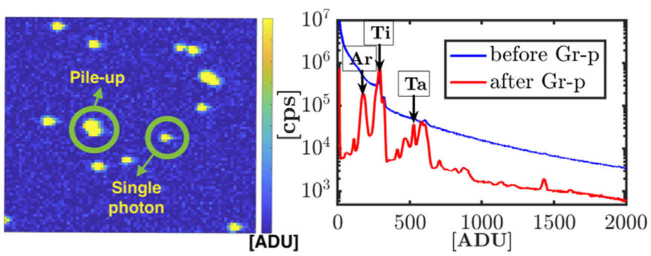

FIG. 4. (Left) Zoomed-in frame showing clusters of pixels in single photon and pileup modes. Energy scale expressed in analog-to-digital units (ADU). (Right) Energy spectrum of single pixel raw data (blue line) compared to the one obtained by grouping post-processed analysis (red line).[15]

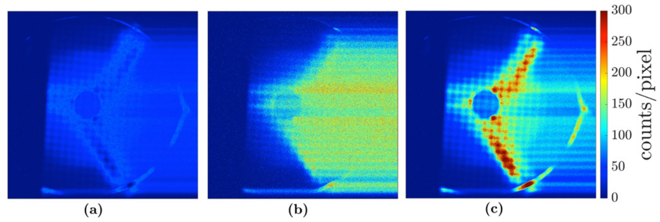

FIG. 5. HDR imaging: (a) long exposure time acquisition, (b) weighted short exposure time acquisition, and (c) HDR final image.

TABLE II. HDR acquisition parameters for short- and long-exposure modes.

Exp. mode	# frames	t_{exp} (s)
Short	1000	0.05
Long	3000	0.7

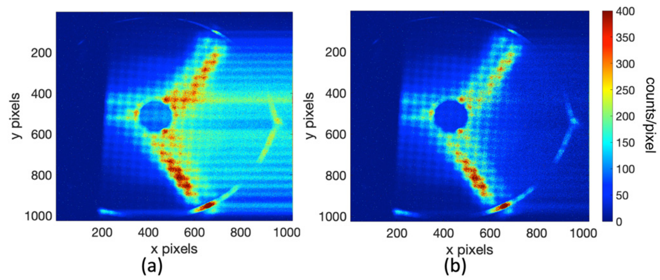

FIG. 6. Effect of the readout effect correction: (a) before and (b) after the application of the algorithm.

A. Benchmark correction of post-processed CCD data

Each photoelectric event on the CCD, once the exposure time is fixed, has a certain probability of being discarded as a multi-photon overlap, depending on the respective cluster size. This scanning (and discarding) of the overlapped clusters, however, due to intrinsic reasons, does not have 100% efficiency.

In order to take into account this effect, and further improving the overall precision of the measurements, we performed some SDD benchmark measurements in the same optical configuration as the CCD camera. The SDD was used to acquire volume-integrated x-ray spectra, under the same optical arrangement of the pinhole camera, just to compare (and renormalize, if needed) the respective spectra. This method led to the evaluation of a second, relative normalization factor which was used to renormalize CCD spectra in addition to the quantum efficiency.

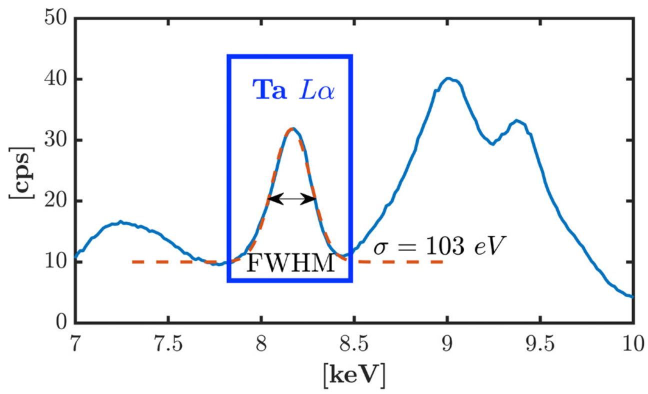

FIG. 7. X-ray spectrum highlighting the $L\alpha$ characteristic line at 8.15 keV. The energy resolution was estimated on this peak by a Gaussian fit ($\sigma = 103$ eV, FWHM $= 242$ eV).

Figure 8 shows the SDD (blue) and CCD (red) spectra with statistical error bands, both renormalized by the respective intrinsic quantum efficiency and absorber transparency (shown in Fig. 3). The two spectra differ from each other due to the presence of spurious, multi-event (i.e., not single photon counted or dimer) peaks, which are only partially discarded by the analysis algorithm. As this effect is negligible on the continuous part of the spectra (as the counting rate is $10 - 100$ times lower), a normalization factor (green dash line) was defined by the ratio of the respective bremsstrahlung spectra (the one collected by the CCD and the other one captured by the SDD), which were then interpolated in the regions free of fluorescence lines. The respective interpolated lines are shown with the same colors (subplot).

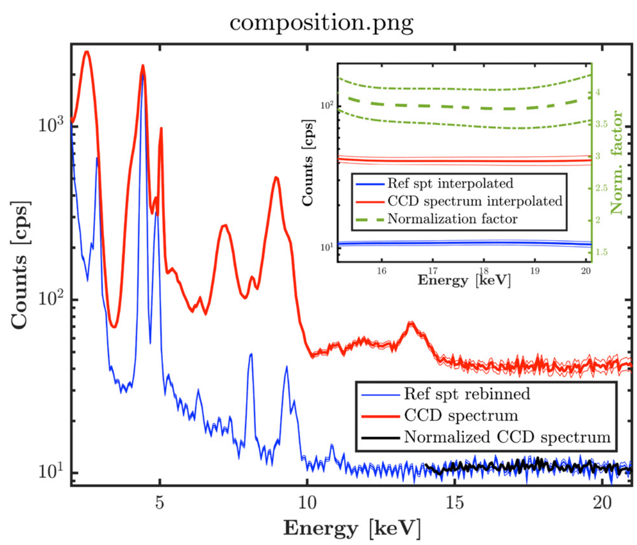

FIG. 8. SDD (blue) and CCD (red) spectra with statistical error bands. The interpolated trends of the continuous parts of the spectra are also shown in the subplot, excluding the fluorescence lines. The ratio between these latter two defines the respective normalization factor (green dash line) with its error band. The renormalized CCD spectrum is shown in black, correctly overlapped with the SDD one.

The application of such an additional normalization to the CCD data yields the black line in the figure, defined only in the region free of fluorescence lines (15–20 keV). This renormalized spectrum coincides, by definition, with the SDD one (blue curve).

This further post-processing provides a more reliable evaluation of the CCD spectral data, allowing to extract realistic physical information from the bremsstrahlung energy spectra, as shown in Sec. VI.

IV. ENERGY-FILTERED HDR IMAGING

Spectral information was collected on each pixel, with a resolution of 242 eV at 8.15 keV. This information can be then re-elaborated in two ways: (1) it can be integrated over user-defined spatial regions of interest (ROIs), in order to obtain the relative ROI-averaged x-ray emission, or (2) it is possible to select some specific energy intervals in order to map the spatial distribution of detected photons corresponding, for instance, to certain characteristic x-ray lines.

Ar-, Ti-, and Ta-filtered maps were obtained by selecting each respective energy range, in order to study the dynamics of plasma confinement and of the axial and radial losses.

Figure 9 shows the total energy spectrum of plasma emission summed up over the whole frame (top), the map of (a) Ar, (b) Ti, and (c) Ta characteristic emissions in different respective pseudo-colors (all the analyzed energy spectra have been re-binned by a factor of 4 with respect to the spectrum shown in Fig. 7). Characteristic fluorescence lines, reported in Table III, are highlighted by the same respective colors on the full-frame energy spectrum (top).

The x-ray emission of the confined Ar plasma is mainly determined by the deep electron–ion ionizing collisions, while the emission from the walls is caused by the deconfined plasma fluxes, especially the fast electrons escaping the magnetic trap and impinging on the chamber walls. Both the in-plasma and on-wall interactions generate both bremsstrahlung and characteristic line emission.

The inspection of the inner volume of the plasma chamber is allowed through the aluminum mesh on the injection flange (having a wire diameter of 400 μm, with a transparency on two thirds of the injection endplate), so that the plasmoid and the extraction flange are

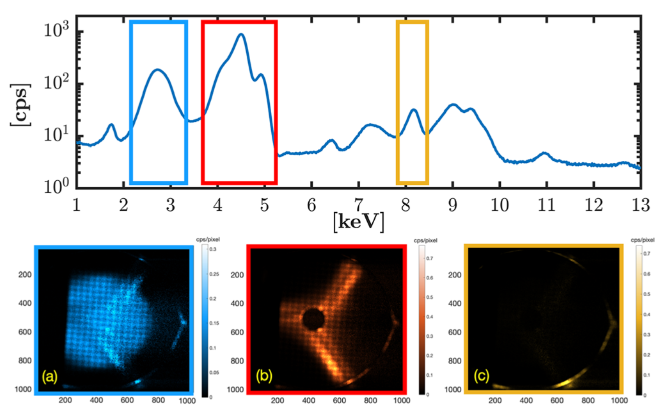

FIG. 9. Energy-filtered images in the x-ray emission ranges of Ar (a), Ti (b), and Ta (c). Characteristic fluorescence lines are highlighted in the spectrum shown on the top, using the same colors of the corresponding images. The pseudo-color scales are obtained by the assignment of different pseudo-colors (blue, red, and yellow) to the respective fluorescence peaks (Ar, Ti, and Ta).

TABLE III. Main characteristic lines selected for plasma elemental imaging.

Element	X-ray line	Energy (keV)
$^{40}_{18}$Ar	$K\alpha_{1,2}$	2.96
$^{40}_{18}$Ar	$K\beta$	3.19
$^{48}_{22}$Ti	$K\alpha_{1,2}$	4.51
$^{48}_{22}$Ti	$K\beta$	4.93
$^{181}_{73}$Ta	$L\alpha_{1,2}$	8.15

clearly visible. All the images are affected by the "shadow" of the aluminum mesh along the line of view, which creates the well-visible regular pattern (shadowed rectangles) as an intensity modulation.

The plasmoid, the extraction flange, and the chamber walls are well visible in the pictures with a spatial resolution of 560 μm, calculated at the center of plasma chamber. The quasi-circular cross section of the plasmoid, well visible in Fig. 9(a), closely resembles the expected ellipsoidal cross section of the ECR surface, defined by the magnetic iso-surface corresponding to the cyclotron resonance $B_{ECR} = (m/q)\omega_{RF}$ [m, q electron mass and charge, ω_{RF} resonant radio frequency, and B_{ECR} magnetic field]. The tri-cuspidal structure (two of the cuspids are well visible, the third one is partially cut by the Al endplate), visible in Fig. 9(b), corresponds to the footprint created by the axially deconfined plasma electrons impinging on the titanium plate, and it is determined by the shape of the confining hexapolar magnetic field at the intersection with the plate. In Fig. 9(c), the same effect is visible in the tantalum lateral wall of the plasma chamber. In this latter case, however, more spots are visible every 60°, corresponding to the similar tri-cuspidal shape toward the injection endplate, rotated 180° as it is usual in a minimum-B magnetic configuration.

Figure 10 shows the image obtained by the overlap of all the three components Ar, Ti, and Ta. Pseudo-colors were balanced in order to make all the components well visible in the picture (the scale of each balanced color is reported in the picture).

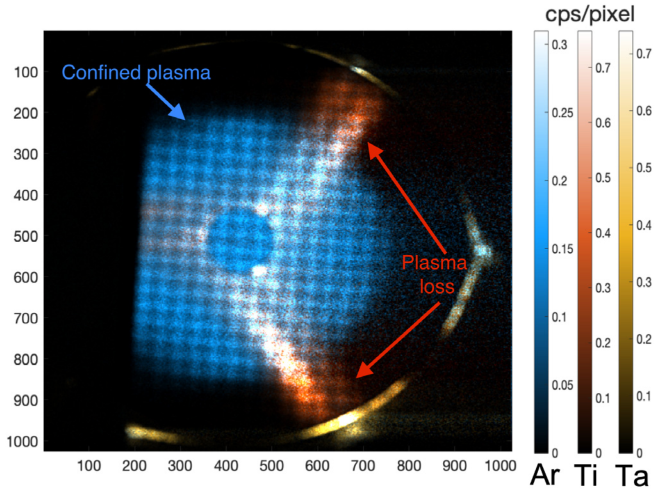

FIG. 10. Pseudo-colors combined image with all the fluorescence components of Ar, Ti, and Ta.

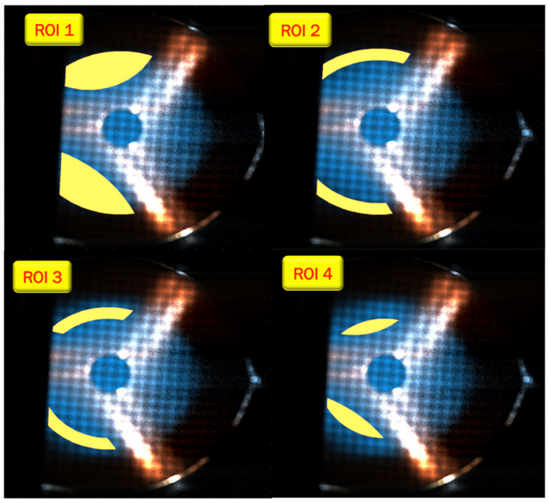

FIG. 11. Set of ROIs selected (yellow shades) on the CCD image: radial sections of plasmoid projection, excluding the titanium emission and the right side of the image, mostly affected by readout residual effect.

V. SPACE-RESOLVED X-RAY SPECTROSCOPY

As mentioned before, the experimental information can be re-elaborated over user-defined spatial ROIs, enabling a selective analysis of ROI-averaged energy spectra.

In this way, a selective analysis of plasma emission only is possible, excluding for instance the contributions from the plasma chamber walls (plasma losses), which can be easily identified as the ones containing the characteristic lines from Ti and Ta (Fig. 9).

A set of ROIs, shown in Fig. 11 was defined to analyze the x-ray spectra in several plasma regions. In particular, circular sections of plasma projections were selected in order to study the radial profile of plasma parameters, assuming the azimuthal symmetry of the plasmoid, which seems to be reasonable looking at the azimuthal integrated emission.

Also the right part of the image was excluded, mostly affected by a residual CCD readout effect, containing some traces of titanium emission.

The ROI extension was maximized in order to minimize the spectral statistical error.

An interesting feature of this method is the possibility of subtracting the x-ray scattering and secondary emission background from the Ti wall of the chamber, assuming its homogeneity over the entire surface and a total transparency of the plasmoid.

The background spectrum was obtained from the "clean" portion of the titanium endplate, as shown in Fig. 12, i.e., the part of the images with no signal coming from neither the plasma nor the electrons' impact on the endplate itself. It was averaged on the respective ROI surface, so it is expressed in [cps/pixel]. This has been done assuming the homogeneity of the scattered x rays by the plasma chamber walls, in particular, by the Ti endplate.

The energy spectra, defined in the respective set of ROIs and subtracted from the background, are shown in Fig. 13.

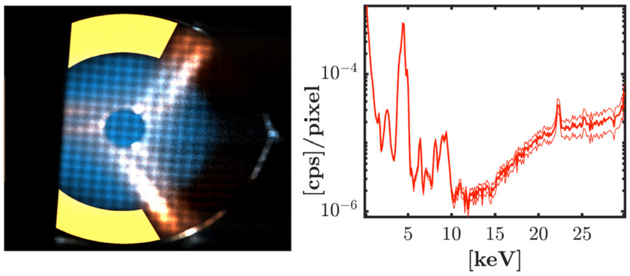

FIG. 12. Background ROI: x-ray-induced emission from the Ti wall (including both scattered and fluorescence radiation).

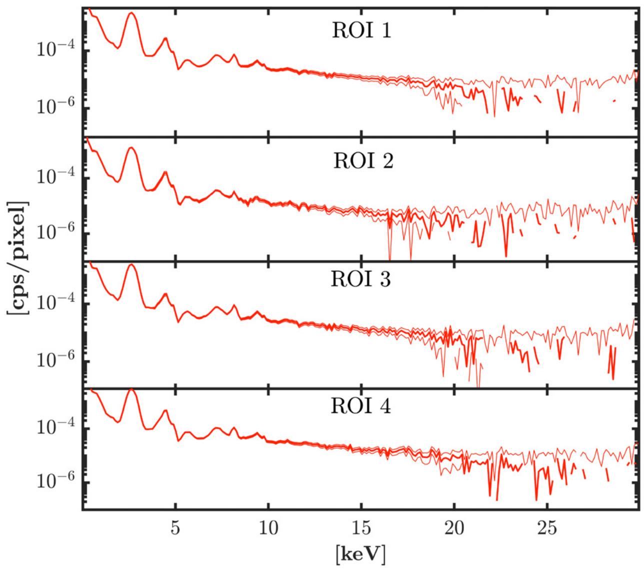

FIG. 13. Energy spectra of the four ROIs, subtracted from the background.

VI. ELECTRON DENSITY AND TEMPERATURE EVALUATION

Therefore, according to a model of plasma emissivity[22] with the assumption of a Maxwell–Boltzmann energy distribution, it is possible to extrapolate the plasma thermodynamic parameters from the experimental emissivity density distribution $J_{\exp}$, defined by the following equation:

$$J_{\exp}(h\nu) = h\nu \frac{N^p(h\nu)}{t} \frac{4\pi}{\Delta E V_P \Omega_g}, \tag{1}$$

where $h\nu$ is the photon energy, $N^p(h\nu)/t$ is the measured counting rate, ΔE is the energy bin width, V_P is the plasma volume, and $\Omega_g/4\pi$ is the geometrical efficiency (defined in each point of the plasma volume as the ratio between the solid angle subtended by the detector and the total emitting angle 4π).

As $J_{\exp}(h\nu)$ is the total x-ray emission from both the bremsstrahlung processes and the fluorescence line emission (XRF), it can be decomposed by the sum of the two respective spectra as follows:

$$J(h\nu) = J_{brem.}(h\nu) + J_{XRF}(h\nu). \tag{2}$$

The expression for the bremsstrahlung emissivity density is then given as

$$J_{brem.}(h\nu) = \rho_e\rho_i h\nu \int_{h\nu}^{\infty} \frac{d\sigma_K(h\nu)}{dh\nu} v_e(E) f(E) dE, \tag{3}$$

where $\rho_e\rho_i$ is the product of the electron and ion density, $v_e(E)$ is the electron speed, $\frac{d\sigma_K(h\nu)}{dh\nu}$ is the differential cross section, and $f(E)$ is the EEDF.

Using Kramer's formula[23] for the differential cross section and the Maxwell–Boltzmann distribution for $f(E)$, the bremsstrahlung emissivity density is described by the following equation:

$$J^{M-B}_{brem.}(h\nu) = \rho_e\rho_i (Z\hbar)^2 \left(\frac{4\alpha}{\sqrt{6m_e}}\right)^3 \sqrt{\frac{\pi}{k_B T_e}} e^{-\frac{h\nu}{k_B T_e}}. \tag{4}$$

A focused effort to develop a method for blending together the analysis from characteristic lines with the continuum of the spectrum by an iterative process is ongoing, and details on this technique will appear in a future publication. However, for the sake of this paper, we will here focus on the continuum only. The expression (4) was, thus, used to fit the bremsstrahlung experimental emissivity density in order to extrapolate the electron temperature and density.

However, this process requires a rigorous determination of the geometrical detection efficiency $\Omega_g/4\pi$ and the effective plasma volume V_P, to be done for each of the selected spatial ROIs in the plasma. For this purpose, a geometrical simulation was required, considering the overall geometry of the pinhole optical system and the plasma chamber setup.

The plasma volume was identified as the region enclosed by the ECR surface, defined by the 3D map of the resonant magnetic region. The local geometrical efficiency was defined for each point of a 3D plasma model as the projection of a given subvolume of the plasma (voxel), projected across the aluminum mesh (hence, assuming its intrinsic transparency) and the pinhole, onto the CCD detector.

Figure 14 shows the aluminum mesh (a), the optical simulation of the plasmoid through it (b), and the equivalent geometrical efficiency projection along the z axis (c).

The emissivity density was studied in the set of ROIs defined in Fig. 11.

Each ROI defined a 3D portion of the plasma on which the volume V and the efficiency $\Omega_g/4\pi$ have been summed.

The resulting emissivity density spectrum for ROI 1 is shown in Fig. 15 (red line). The blue line reports the weighted fit of $J^{M-B}_{bremss}(h\nu)$ (4), constrained in the range of 10–16 keV (green line).

Table IV and Fig. 16 report the extrapolated values of temperature and density in all the 4 ROIs, with respective error bars calculated by the experimental error propagation into the fit parameters.

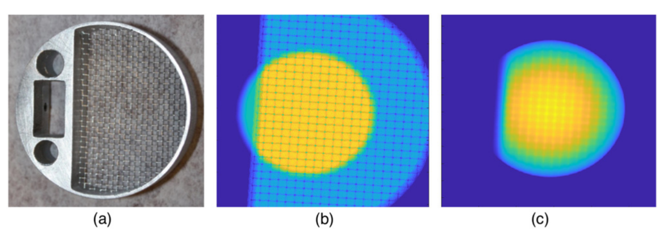

FIG. 14. (a) Aluminum mesh, (b) optical simulation of plasmoid with the mesh, and (c) geometrical efficiency projection along the z axis.

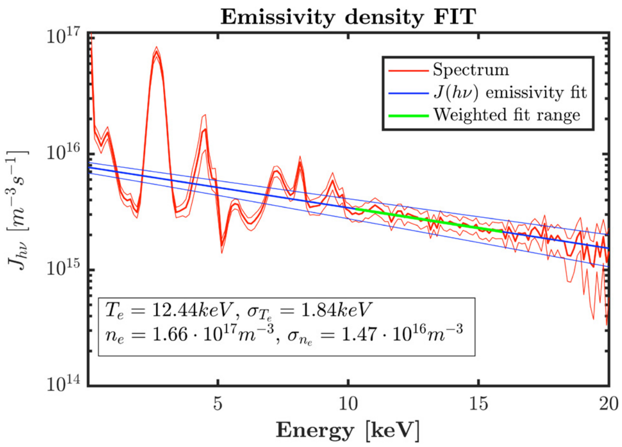

FIG. 15. Emissivity density spectrum $J_{exp}(h\nu)$ in ROI 1 (red line); Maxwell–Boltzmann emissivity fit $J^{M-B}_{bremss}(h\nu)$ with respective error bars (blue line); and fit range (green line). Temperature and density extrapolation is reported below.

TABLE IV. Plasma electron temperature and density results, extracted in the four ROIs.

	Temperature (keV)	Density (m^{-3})
ROI 1	12.44 ± 1.84	$(1.66 \pm 0.15) \times 10^{17}$
ROI 2	12.10 ± 2.54	$(1.36 \pm 0.16) \times 10^{17}$
ROI 3	12.67 ± 2.60	$(1.71 \pm 0.27) \times 10^{17}$
ROI 4	12.01 ± 2.51	$(1.83 \pm 0.25) \times 10^{17}$

The plasma electron density and temperature have been extracted with a precision between 9%–16% and 15%–21%, respectively, allowing a preliminary characterization of the plasma temperature and density profile.

In particular, the temperature shows a constant trend with an average value of ~ 12.3 keV in all the selected ROIs. The density profile decreases going from the inner region (ROI 4) to the external one (ROI 2), especially selected on the border of the plasmoid projection. The average values are measured in ROI 1.

As the experimental error is mostly dependent on the spectrum intensity, the measurement can be, in principle, improved by extending the total measurement time and/or the spatial ROI dimensions in a trade-off between parameter extrapolation accuracy, measurement time, and space resolution.

Furthermore, the results are model dependent: their significance depends on how the EEDF matches with the Maxwell–Boltzmann distribution. As mentioned above, further upgrades on the model are still under development, by implementing different distribution functions on a simulated plasma environment and blending information coming from line emission part also.[22]

VII. DISCUSSION

The spatially resolved spectral analysis here shown represents a relevant step forward enabling the study, for the first time, of the local ECR plasma parameters.

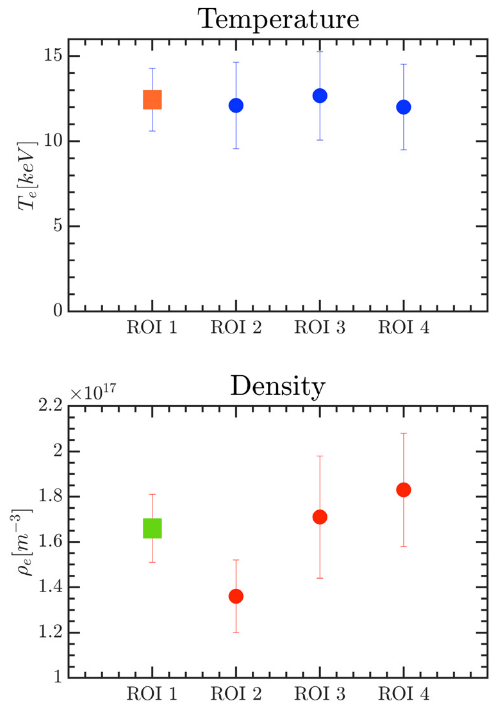

FIG. 16. Plasma electron temperature and density results, extracted in the four ROIs. ROIs 2–4 (circles) go from plasmoid edge toward the axis; ROI 1 (square in different color) represents, in short, a kind of space average of ROIs 2–4.

We would now analyze our outcomes in comparison with the ones already available in the literature, depending on the different techniques and approaches mentioned in the introduction section. For this purpose, we have arranged the summary illustrated in Table V. The differences were highlighted in terms of the observables that can be measured, including the advantages and limits of each technique, and compared them with the contents of this paper.

X-ray volumetric spectroscopy has been largely used for characterizing both hot (using scintillators or HPGe detectors, being sensitive above 100 keV) and warm (2–30 keV) electron populations. To cope with the mentioned limitation due to the superposition of plasma- and wall-emitted radiation, properly designed collimators were often used, in order to suppress the photon flux coming from the chamber walls. This allowed us to get—in some cases—volume-integrated T_e and n_e average values. The advantage of this simple technique consists of prompt output and easy analysis, although the latter is model dependent. Some experiments in which the direct estimation of density and temperature was performed are mentioned in Table V, line A. They were mostly carried out at INFN-LNS, at the GSI-Darmstadt, and at the Atomki–Debrecen,[18,24] by applying an emissivity model as reported in Gumberidze *et al.*[5]

For example, according to the experimental findings of Mascali *et al.*,[18] typically estimated warm electron temperatures and densities (obtained in the 2–30 keV energy domain in ECRIS operating at 13–14 GHz and 30 W) lie in the ranges of 16–22 keV and $3.0–5.5 \times 10^{16}$ m^{-3}, respectively, with an experimental error ranging 5%–10 %.

TABLE V. Summary of plasma x-ray diagnostic techniques.

	Diagnostic	Energy-res.	Space-res.	Observable	Main features	References
(A)	**Volumetric spectroscopy**	×		Volumetric T_e, n_e; chemical analysis	Prompt output; model dependance	2–5, 10, 18, and 24
(B)	**Energy-integrated imaging**		×	Plasma structure	Prompt output; fast analysis	8, 9, 17, 18, and 26
(C)	**Energy-resolved imaging**	×	×	Plasma structure; local chemical analysis	Long measurement time; advanced analysis	6, 9, 14, and 16
(D)	**Energy-resolved imaging + interpretative model**	×	×	Local T_e, n_e; plasma structure	Long measurement time; advanced analysis; model dependance	This work

Typical values for the hot plasma, regarding again T_e and n_e, were found in Mascali *et al.*[24] in the ranges of 15–35 keV and $1-5\times10^{16}\,\mathrm{m}^{-3}$, working with 20–200 W of RF power. Concerning the hot plasma component, several other experiments were carried out in different plasma conditions, operating on more powerful ECRIS setups, and providing temperature estimates in the range of $10-100$ keV. In particular, Thuillier *et al.*[10] report on the different techniques adopted to estimate the spectral temperatures in various ECR setups vs RF power, gas pressure, and magnetic field profile. We here mention, for the sake of an example, the values reported in Barué *et al.*,[25] which were benchmarked, as for the hot electrons, by ECE (electron cyclotron emission) simultaneous measurements. They obtained a pretty good agreement by using, as the x-ray detector, a HpGe system, operating on a 18 GHz ECRIS. Temperature values spanned from around 100 keV at lower pressures (10^{-5}mbar) and higher RF power (above 400 W) down to 40 keV at higher pressures and lower RF power (100 W). In a setup able to vary the pumping frequency from 18 to 28 GHz, i.e., the VENUS source at LNBL,[2] they obtained spectral temperatures ranging from 20 to 100 keV for the hot electrons; the variation was dominated by the tuning of the $B_{\min}$ field more than the pumping wave frequency.

The work on x-ray imaging and spectroscopy techniques has been initiated by our teams around 20 years ago (see, for instance, Refs. 9, 14, and 18) and the same techniques have been used also in other plasma-based facilities such as at Z-machines[8] or in plasma fusion devices.[26] The energy-integrated imaging technique (Table V, line B) gives access to the spatial features of plasma.

Operating in a spectrally integrated mode, i.e., using a long exposure time where multi-events are accumulated by the camera, despite the energy discrimination of the single events is not possible, the local energy content (basically, the product of density and temperature) of the plasma can be evaluated.

The advantage is that these acquisitions are relatively fast (tens of seconds) and, thus, it is possible to master, likely "online," any change in the plasma structures or to monitor losses on the plasma chamber walls. Studies on the change in the plasma structure vs different operative configurations (in terms of magnetic field, RF pumping frequency and power, plasma heating mode, etc.) were carried out. In addition, space-resolved morphological analysis of plasma confinement[17] allows to distinguish the spatial distribution of plasma anisotropy: confined and deconfined plasma, respectively, located inside the ECR surface and into the loss regions (magnetic branches), can be studied separately. It was also demonstrated that the plasma density distribution can be rearranged by a new plasma heating mode [i.e., the TCFH (two-close-frequency heating)], becoming denser in the central region of the plasma chamber.

The combination of x-ray imaging and spectroscopy through the SPhC analysis (Table V, line C) enables to investigate local plasma properties. Being rather complex to be applied, it still has very limited background literature to be accounted for. The first attempt to provide a 2D map of emitted x rays from an ECRIS in a spectrally resolved way dates back to 2017.[14] However, there the investigation was limited to the spatial structure of the Ar plasma, just distinguishing it from the endplate emission, and also focusing on the conditions under which the so-called plasma "hollowness"—namely, the depletion of the central regions of the plasmoid—was more evident (which may explain a typical inefficiency observed in the ECRIS beam extraction).

Both the experimental setup[27] and the analytical method[15] have been improved since then. In this respect, here we have shown the obtained SPhC images in HDR mode. This operational mode has the well-known disadvantage of very long measurement times (even several hours for some configurations) and also requiring a sophisticated post-processing algorithm to extract the quantitative information. However, on the other side, this is the only way to get local quantitative plasma parameter estimates. The first analysis was based on the specific fluorescence lines of each material of the plasma chamber and of the in-plasma ions, without any model-based fitting procedures, and was published in 2022.[16] It was anyway possible to get a spatially resolved characterization of plasma-emitted vs plasma chamber wall-emitted spectra.

In the present work (Table V, line D), we implemented a significant advancement in terms of SPhC data post-processing. The space-resolved information allowed us to select plasma regions where a spectroscopic analysis could be performed, discarding, for instance, those regions involved in the plasma deconfinement phenomenon. Moreover, it allowed us to reconstruct and subtract the x-ray scattering background spectral contribution from the plasma chamber wall, reducing such a relevant source of uncertainty.

Therefore, interpretative models[5,22] were applied to the space-resolved spectral information to get local estimations of plasma parameters, as never done in the past.

The present results give now important features about the ECR plasma structure and confinement.

First, the plasma temperature results to be almost constant over the whole confinement volume, at least within the experimental error

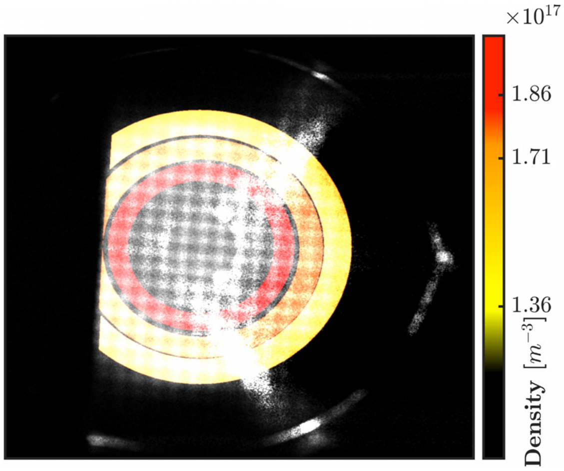

FIG. 17. Plasma electron density map in pseudo-color scale (overlapped on the B-W plasma image), obtained by extrapolating ROIs 2, 3, and 4 over respective circular crowns, in the assumption of a spherical symmetry of the system.

($\sim$ 10% − 25%), suggesting a smooth distribution of every physical quantities related to it. The radial density profile shows a smooth but clear trend, compatible with a confinement gradient toward the internal regions of the plasmoid. In particular, data of ROI 2 show a slight drop, highlighting the transition region from the plasmoid to the plasma–halo, as suggested by Ivanov *et al.*:[28] a density 40% lower is measured in proximity of the ECR edge, outside of which the x-ray emission flux is almost zero and so the plasma is practically absent.

An extrapolation can be reasonably done to define temperature and density in regions not directly measurable, by extending the ROIs over the respective axis-symmetrical regions, according to the symmetry of the magnetic field inside the ECR surface.

The resulting density map is shown in Fig. 17, highlighting its gradient in a pseudo-color scale.

It is, therefore, reasonable to identify the ECR surface as a kind of separatrix, i.e., the boundary between two domains separating the plasma core from the rarefied halo.

The RF ignition power results in being released into the small volume of $\sim 2\,\mathrm{cm}^3$, enclosed by the ECR surface, giving a power density of $\sim 100\,\mathrm{W/cm}^3$ (part of this power is then released into plasma losses).

The comparison of such results with the volumetric ones (Table V, line A) highlights the limits of the latter, due to the aforementioned difficulty in the deconvolution of plasma and chamber wall contributions. In general, our local estimate of plasma temperatures, at least for the warm component, indicates a lower value than the one estimated by volumetric measurements.

If, for the sake of comparison, we consider the volumetric measurements in Atomki–Debrecen in the 13–14 GHz range at 30 W, i.e., the ones reported in, Ref. 18, we observe in this current paper a relevant increase in the density estimates (3.0–$5.5 \times 10^{16}\,\mathrm{m}^{-3}$ in volumetric measurements, compared to 1.4–$1.9 \times 10^{17}\,\mathrm{m}^{-3}$, in this work) that could be in principle related to the different ignition power (30 W vs 200 W), while the temperature is deemed to be lower than the estimates from volumetric measurements when using the local estimation mode (this paper), despite the higher RF power.

The reason for this latter discrepancy could be linked to the experimental technique. Despite the good collimation in the volumetric measurements, in fact, it could not be excluded that a small contribution to the collected spectra came from the deconfined plasma. This was in fact confirmed by the presence of Fe and Cr fluorescence peaks in the collected spectra.

VIII. CONCLUSION

The first experimental results of local plasma parameters (electron density and temperature) evaluated by a CCD-based pinhole camera for x-ray spectroscopy and imaging are reported here. Energy-resolved imaging made possible the study of elemental space distribution, giving information about plasma structure and confinement dynamics with a space resolution of 560 μm and an energy resolution of 242 eV at 8.15 keV. Local plasma parameter evaluation was performed by the application of an emissivity model on post-processed space-resolved spectra, with a precision of $\sim$ 10%–25%, under the assumption of Maxwell–Boltzmann EEDF distribution. The obtained densities and temperature were compared to the ones estimated in other ECR setups in the past, commenting about the advantage of using a fully space-resolved technique with respect to the volumetric measurements performed so far.

These first direct evaluations of space-resolved plasma parameters have shown the clear formation of a plasmoid–halo structure inside the plasma chamber, i.e., the dense and energetic plasma is substantially confined inside the magnetic iso-surface corresponding to the ECR layer. Therein, the plasma is almost uniformly distributed in both density and temperature, except the near-plasmoid-edge region, where the density drops to around 40%. In the plasma–halo, the x-ray emission is comparable with the background noise, except for the cusp structures corresponding to the magnetic branches along which the electrons flow away and impact the plasma chamber walls and endplates.

Ongoing activities are focused on the development of a fast x-ray shutter in order to overcome the critical issue of the CCD readout noise, now demanding a complex post-processing of the acquired data, and to improve the method toward a time-resolved performance. In addition, a new interpretative model is under development[22] to constrain thermodynamic parameter extrapolation with the x-ray fluorescence data.

ACKNOWLEDGMENTS

The authors gratefully acknowledge the support of INFN by the Grants PANDORA (5th Nat. Comm.) and PANDORA_Gr3 (3rd Nat. Comm.). This work has been partially funded by the European Union (NextGeneration EU), through the MUR-PNRR project SAMOTHRACE (No. ECS00000022) and the MUR-PNRR project NQSTI (No. PE0000023).

AUTHOR DECLARATIONS

Conflict of Interest

The authors have no conflicts to disclose.

Author Contributions

G. Finocchiaro: Formal analysis (equal); Investigation (equal); Methodology (equal); Software (equal); Validation (equal);

Visualization (equal); Writing – original draft (equal). **E. Naselli:** Conceptualization (equal); Data curation (equal); Formal analysis (equal); Investigation (equal); Methodology (equal); Resources (equal); Software (equal); Supervision (equal); Validation (equal); Visualization (equal); Writing – review & editing (equal). **B. Mishra:** Conceptualization (equal); Methodology (equal); Software (equal); Validation (equal). **S. Biri:** Methodology (equal); Resources (equal); Software (equal). **M. Mazzaglia:** Data curation (equal); Methodology (equal). **A. Pidatella:** Conceptualization (equal); Data curation (equal); Investigation (equal); Methodology (equal); Software (equal); Supervision (equal); Validation (equal); Writing – review & editing (equal). **R. Rácz:** Data curation (equal); Formal analysis (equal); Investigation (equal); Methodology (equal); Resources (equal); Software (equal). **G. Torrisi:** Data curation (equal). **D. Mascali:** Conceptualization (equal); Data curation (equal); Formal analysis (equal); Funding acquisition (equal); Investigation (equal); Methodology (equal); Project administration (equal); Resources (equal); Software (equal); Supervision (equal); Validation (equal); Visualization (equal); Writing – review & editing (equal).

DATA AVAILABILITY

The data that support the findings of this study are available from the corresponding author upon reasonable request.

REFERENCES

[1]U. Fantz and O. Tarvainen, Rev. Sci. Instrum. **93**, 101601 (2022).
[2]J. Benitez, C. Lyneis, L. Phair, D. Todd, and D. Xie, IEEE Trans. Plasma Sci. **45**, 1746 (2017).
[3]T. Ropponen, O. Tarvainen, I. Izotov, J. Noland, V. Toivanen, G. Machicoane, D. Leitner, H. Koivisto, T. Kalvas, P. Peura, P. Jones, V. Skalyga, and V. Zorin, Plasma Sources Sci. Technol. **20**, 055007 (2011).
[4]B. Isherwood and G. Machicoane, Rev. Sci. Instrum. **91**, 025104 (2020).
[5]A. Gumberidze, M. Trassinelli, N. Adrouche, C. Szabo, P. Indelicato, F. Haranger, J.-M. Isac, E. Lamour, E.-O. L. Bigot, J. Mérot, C. Prigent, J.-P. Rozet, and D. Vernhet, Rev. Sci. Instrum. **81**, 033303 (2010).
[6]E. Takács, B. Radics, C. I. Szabó, S. Biri, L. T. Hudson, J. Imrek, B. Juhász, T. Suta, A. Valek, and J. Pálinkás, Nucl. Instrum. Methods Phys. Res., Sect. B **235**, 120–125 (2005).
[7]M. Anton *et al.*, Plasma Phys. Controlled Fusion **38**, 1849 (1996).
[8]L. A. McPherson, D. J. Ampleford, C. A. Coverdale, J. W. Argo, A. C. Owen, and D. M. Jaramillo, Rev. Sci. Instrum. **87**, 063502 (2016).
[9]S. Biri, A. Valek, T. Suta, E. Takács, C. Szabó, L. T. Hudson, B. Radics, J. Imrek, B. Juhász, and J. Pálinkás, Rev. Sci. Instrum. **75**, 1420 (2004).
[10]T. Thuillier, J. Benitez, S. Biri, and R. Rácz, Rev. Sci. Instrum. **93**, 021102 (2022).
[11]I. Izotov, O. Tarvainen, V. Skalyga, D. Mansfeld, T. Kalvas, H. Koivisto, and R. Kronholm, Plasma Sources Sci. Technol. **27**, 025012 (2018).
[12]E. Naselli, D. Mascali, S. Biri, C. Caliri, G. Castro, L. Celona, L. Cosentino, A. Galatà, S. Gammino, M. Giarrusso, F. Leone, M. Mazzaglia, R. Rácz, R. Reitano, F. Romano, and G. Torrisi, J. Instrum. **14**, C10008 (2019).
[13]K. Bernhardi and K. Wiesemann, Rev Sci Instrum. **83**(2), 02A337 (2012).
[14]R. Rácz, D. Mascali, S. Biri, C. Caliri, G. Castro, A. Galatà, S. Gammino, L. Neri, J. Pálinkás, F. P. Romano, and G. Torrisi, Plasma Sources Sci. Technol. **26**, 075011 (2017).
[15]E. Naselli, R. Rácz, S. Biri, M. Mazzaglia, L. Celona, S. Gammino, G. Torrisi, Z. Perduk, A. Galatà, and D. Mascali, Condens. Matter **7**(1), 5 (2022).
[16]E. Naselli, R. Rácz, S. Biri, M. Mazzaglia, A. Galatà, L. Celona, S. Gammino, G. Torrisi, and D. Mascali, J. Instrum. **17**, C01009 (2022).
[17]D. Mascali, E. Naselli, R. Rácz, S. Biri, L. Celona, A. Galatà, S. Gammino, M. Mazzaglia, and G. Torrisi, Plasma Phys. Controlled Fusion **64**, 035020 (2022).
[18]D. Mascali, G. Castro, S. Biri, R. Rácz, J. Pálinkás, C. Caliri, L. Celona, L. Neri, F. P. Romano, G. Torrisi, and S. Gammino, Rev. Sci. Instrum. **87**, 02A510 (2016).
[19]S. Biri, R. Rácz, and J. Pálinkás, Rev. Sci. Instrum. **83**, 02A341 (2012).
[20]M. Vasin, Y. V. Ignatiev, A. Lakhtukov, A. Morovov, and V. Nazarov, Spectrochim. Acta, Part B **62**, 648–653 (2007).
[21]L. K. Townsley, P. S. Broos, G. Chartas, E. Moskalenko, J. A. Nousek, and G. G. Pavlov, Nucl. Instrum. Methods Phys. Res., Sect. A **486**, 716–750 (2002).
[22]B. Mishra, A. Pidatella, S. Biri, A. Galatà, E. Naselli, R. Rácz, G. Torrisi, and D. Mascali, Phys. Plasmas **28**, 102509 (2021).
[23]H. Kramers, London, Edinburgh Dublin Philos. Mag. J. Sci. **46**(275), 836–871 (1923).
[24]D. Mascali, L. Celona, F. Maimone, J. Maeder, G. Castro, F. P. Romano, A. Musumarra, C. Altana, C. Caliri, G. Torrisi, L. Neri, S. Gammino, K. Tinschert, K. P. Spaedtke, J. Rossbach, R. Lang, and G. Ciavola, Rev. Sci. Instrum. **85**, 02A956 (2014).
[25]C. Barué, M. Lamoureux, P. Briand, A. Girard, and G. Melin, J. Appl. Phys. **76**, 2662 (1994).
[26]R. Petrasso, M. Gerassimenko, F. H. Seguin, J. Ting, R. Krogstad, P. Gauthier, W. Hamilton, A. T. Ramsey, P. Burstein, and R. Granetz, Rev. Sci. Instrum. **51**, 585–590 (1980).
[27]S. Biri, R. Rácz, Z. Perduk, J. Pálinkás, E. Naselli, M. Mazzaglia, G. Torrisi, G. Castro, L. Celona, S. Gammino, A. Galatá, F. Romano, C. Caliri, and D. Mascali, J. Instrum. **16**, P03003 (2021).
[28]A. A. Ivanov and K. Wiesemann, IEEE Trans. Plasma Sci. **33**, 1743–1762 (2005).